https://doi.org/10.3311/PPme.38117
Creative Commons Attribution

Periodica Polytechnica Mechanical Engineering, 69(1), pp. 1–9, 2025

An Experimental Assessment and Numerical Simulation of the Corrosion Behavior of Aluminum Welded Joints in Diverse Environments

Mortadha Kareem Abdulrazzaq[1*], Hamid Al-Abboodi[1], Hussein K. A. Zahra[2], Taha Hassan Abood[3], Adnan Naama Abood[3]

[1] Kut Technical Institute, Middle Technical University, 10001 Baghdad, Iraq
[2] Maysan Oil Training Institute, 62001 Maysan, Iraq
[3] Technical Engineering College, Baghdad, Middle Technical University, 10001 Baghdad, Iraq
[*] Corresponding author, e-mail: mortadha.kareem@mtu.edu.iq

Received: 15 August 2024, Accepted: 13 January 2025, Published online: 22 January 2025

Abstract

The corrosion behavior of stud-welded AA5083-H321/AA6061-T6 joints was examined. The electrochemical demeanor of the resultant joint was scrutinized in 3.5% NaCl, ASTM seawater, and Na_2SO_4 solutions using scanning electron microscopy (SEM), optical microscopy (OM), energy-dispersive X-ray spectroscopy (EDX), and X-ray diffraction (XRD). COMSOL Multiphysics version 5.6 software was used to predict the galvanic corrosion of AA5083-H321/A6061-T6 in different solutions, using the software finite element (FE) kit. The results indicated that drawn arc stud welding (DASW) enhanced the corrosion resistance of the welding zone, with the highest resistance observed in the Na_2SO_4 solution. This process also influenced the pitting corrosion rate and minimized alterations in pit morphology, with the order of corrosion resistance decreasing from Na_2SO_4 to 3.5% NaCl and ASTM seawater. Among the base metals, the AA6061-T6 side of the weld exhibited superior corrosion resistance compared to the AA5083-H321 side across all tested solutions. The results from the numerical simulation of the corrosion behavior of the welded joint support the experimental assessment.

Keywords

corrosion behavior, AA5083-H321/AA6061-T6, seawater, COMSOL, pitting corrosion

1 Introduction

Aluminum and its alloys are vastly used in various industries because their outstanding properties, such as corrosion reluctance, conductivity of electrical and thermal, good technological properties, e.g., weldability, machinability, and castability, and a high strength-to-weight ratio [1–6]. For instance, 5xxx and 6xxx aluminum alloys are employed in shipbuilding and marine construction due to their corrosion resistance and mechanical characteristics [7, 8]. Corrosion is a significant challenge that affects the performance and durability of materials and coatings across various industries [9, 10]. Thus, understanding the corrosion demeanor of dissimilar welded joints in distinct environments becomes essential for ensuring the structural integrity and longevity of joints using aluminum alloys [11–13]. The corrosion behavior of welded joints is affected by factors of several, including the welding technique (e.g., arc welding, friction stir welding), welding parameters, and exposure conditions. Various types of corrosion can take place in aluminum welded joints, including pitting corrosion, stress corrosion cracking, galvanic corrosion, and crevice corrosion. The severity of corrosion can vary reliant on the specific environment, such as industrial, marine, or atmospheric conditions [14–17].

To assess the corrosion behavior of welded joints, several methodologies and techniques are commonly employed, including electrochemical tests such as electrochemical impedance spectroscopy (EIS), potentiodynamic scanning, and polarization curves. These techniques provide valuable information about corrosion rates, corrosion mechanisms, and the effectiveness of corrosion protection measures [18–21].

The use of aluminum alloys can introduce significant risks during welding as these alloys exhibit differences in their mechanical and chemical properties [22, 23]. Nonetheless, the welding of diverse aluminum alloys is a widely used approach in many applications [24]. Arc stud welding (ASW) is a popular method in different production

Cite this article as: Abdulrazzaq, M. K., Al-Abboodi, H., Zahra, H. K. A., Abood, T. H., Abood, A. N. "An Experimental Assessment and Numerical Simulation of the Corrosion Behavior of Aluminum Welded Joints in Diverse Environments", Periodica Polytechnica Mechanical Engineering, 69(1), pp. 1–9, 2025. https://doi.org/10.3311/PPme.38117

areas, particularly in automotive production, steam boiler production, shipbuilding, bridge construction, and aerospace applications [25]. In the ASW process, an electric arc melts the end of a stud and the surface of a plate workpiece, fusing them together. Aluminum alloys are well suited for ASW, because of their ability to form strong welded joints and their relatively low melting points [26–28].

The impact of various factors on the corrosion characteristics of aluminium weldments has been studied by numerous researchers [6, 29–33]. The effects of heat treatment on the corrosion behaviour and microstructure of AA6061-T6 welded joints in 3.5% NaCl were examined by Nikseresht et al. [28]. The authors came to the conclusion that secondary phases make both the weld metal and the base metal more vulnerable to localised corrosion, while the weld metal zone functions as a cathode and exhibits superior corrosion resistance under various circumstances. Liu et al. [29] investigated the preparation of bulk 6061 aluminum alloy using cold spray-friction stir processing composite additive manufacturing (CFAM). The study involved characterizing the microstructures of cold-sprayed (CS) and CFAM samples through optical microscopy (OM), scanning electron microscopy (SEM), and electron backscatter diffraction (EBSD). Mechanical properties and corrosion behavior were assessed using microhardness, tensile, and corrosion tests. The impact of the microstructure on the corrosion resistance of TIG-welded AA1579 in 0.6 M NaCl was investigated by Gnedenkov et al. [30]. In contrast to the foundation material and the fusion zone, they demonstrated that the heat-affected zone is more susceptible to localised corrosion. Liu et al. [31] used gas tungsten arc welding (GTAW) to examine the nugget zone's resistance to corrosion in AA2519-T87 friction stir welded joints. They discovered that GTAW greatly improves the nugget zone's resistance to corrosion, resulting in a 14.5% improvement in polarisation resistance and a 59.6% decrease in maximum corrosion depth. FSW-GTAW decreases the area fraction of coarse intermetallic compounds, leading to a decrease in electrochemical activity, which consequently enhances the corrosion resistance of the nugget zone. However, as yet there has been no research on the corrosion characteristics of aluminum alloys welded using DASW.

This study investigates the effects of the ASW process on the corrosion behavior of aluminum welded joints in different corrosion environments. Specifically, it examines the corrosion resistance of AA5083-H321/AA6061-T6-T6 stud welded joints in seawater, NaCl, and Na2SO4. The microstructural changes that occur during corrosion are analyzed using various techniques, including optical microscopy, SEM, EDX, and XRD. COMSOL Multiphysics software 5.6 is used to simulate the experimental test to understand the galvanic corrosion.

2 Experimental work

Plates of AA5083-H321 (composition: 0.39% Si, 0.36% Fe, 0.10% Cu, 0.90% Mn, 4.50% Mg, 0.20% Cr, 0.18% Zn, 0.07% Ti, balance Al) were welded to stud of AA6061-T6-T6 (composition: 0.75% Si, 0.235% Fe, 0.165% Cu, 0.12% Mn, 0.864% Mg, 0.042% Cr, 0.092% Zn, 0.017% Ti, balance Al) using the DASW process. The welding conditions (200 A welding current, 0.2 second welding time, and 20 L/min gas flow rate) were taken from Razzaq [27], offering a maximum torque strength. Fig. 1 presents a schematic view of the cross-section of a dissimilar DASW joint.

The samples were prepared in conformity with the standard electrochemical corrosion testing protocols prior to the corrosion test. On SiC paper ranging from grade 240 to grade 3000, the samples were ground with water and subsequently polished using a lapping cloth that used a 3-0.1 μm diamond. The AA6061-T6 stud, AA5083-H321 plate, and dissimilar weldments were tested for corrosion behaviour at room temperature in ASTM sea water, 3.5% NaCl, and 0.5M Na2So4 solution. The appearance and distribution of the corrosion products on the specimens' surfaces were checked using an optical microscope (OM). A scanning electron microscope (SEM) fitted with an energy-dispersive X-ray analysis unit (EDX) was used to examine a few specimens in order to ascertain the morphology and chemical makeup of the corrosion products that developed on their surfaces. X-ray diffraction (XRD) analysis was performed to identify the crystal structure of the corrosion products.

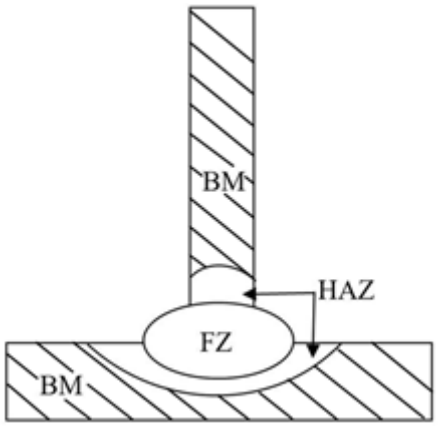

Fig. 1 Cross-section of DASW joint of AA5083-H321/AA6061-T6

An electrochemical workstation (Model CHI 604E, CH Instruments, China) was used to measure the potentiodynamic polarisation curve. The working electrodes were polished examples. As a reference electrode, Ag/AgCl saturated with KCl was employed. The potentiodynamic polarisation curve was measured after the sample was submerged in the test solution for roughly half an hour, or until the sample surface stabilised. The open circuit potential (OCP) was taken into account when setting the applied potential range, and the potentiodynamic polarisation curve scan rate was 0.01 V/sec. To understand galvanic corrosion, the experimental test was simulated using COMSOL Multiphysics software 5.6.

3 Results and discussion

This study evaluated the corrosion behavior of AA5083-H321, AA6061-T6 base metal, and dissimilar welded joints using an electrochemical corrosion method in three different electrolyte solutions, namely ASTM seawater, NaCl, and Na_2SO_4.

3.1 Microstructure analysis

A microstructure analysis of the AA5083-H321/AA6061-T6 weldments was carried out before and after the corrosion testing. Fig. 2 shows the microstructure of the different regions before the corrosion test. The SEM shows a cellular dendritic structure at the center of the fusion zone, and more columnar dendritic with equiaxed zones have formed at the welding interface. Additionally, the welding surface is homogenous and shows no defects.

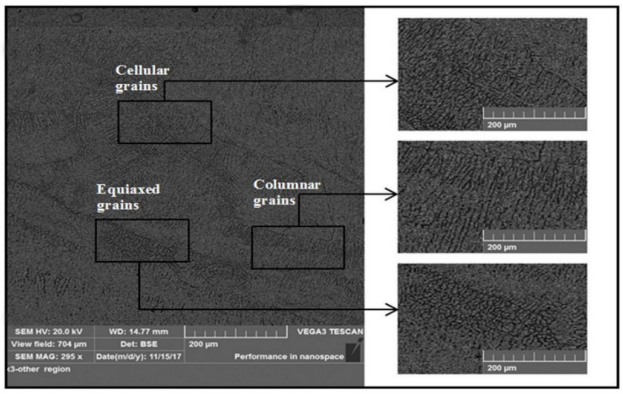

Fig. 2 Microstructure of dissimilar welded joint before corrosion test

Following the electrochemical polarization test, pitting – a localized corrosion onslaught – was seen on the surface of the base metal and welded joints in all settings. This suggests that ions like sulfate and chloride play a key part in the corrosion process, as illustrated in Fig. 3.

The presence of chloride in ASTM seawater was found to accelerate the corrosion rate, leading to the formation of deeper and larger pits compared to sulfate ions. In contrast, the Na_2SO_4 solution exhibited the lowest corrosion rate due to lower concentrations of chloride ions (see Table 1). Figs. 3 and 4 demonstrate how ASTM seawater was more aggressive than NaCl and Na_2SO_4 in terms of pitting corrosion, resulting in greater pit sizes and more severe localized corrosion, as confirmed by the OM analysis.

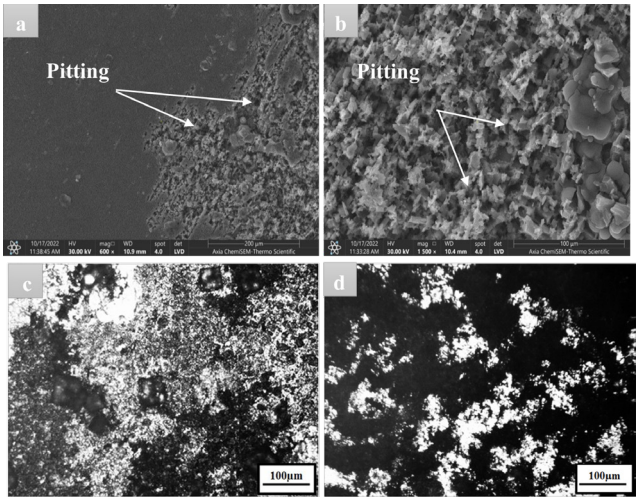

Fig. 3 SEM & OM of dissimilar welded joint after corrosion test in ASTM sea water (a) pitting region at a lower magnification (600×), b) pitting region at a higher magnification (1500×), (c) AA5083 plate, (d) AA6061-T6 stud

Table 1 Potential characteristic of parent aluminum alloy and welded joints

Chemical Solutions	ITEM	E corr. (volt)	I corr. (Amp.)	Corr. Rate mmpy	Epp (volt)	Eb (volt)	ipp (Amp.)	OCP (volt)
ASTM Sea Water	5083	−1.237	9.215×10^{-5}	1.041	−1.161	−0.8	1.140×10^{-4}	−1.205
	6061	−1.517	4.753×10^{-5}	0.756	−1.532	−0.8	5.128×10^{-5}	−1.174
	weld	−1.076	3.100×10^{-6}	8.969×10^{-2}	−1.0	−0.75	2.326×10^{-5}	−1.116
NaCl 3.5%	5083	−0.872	2.259×10^{-5}	2.255×10^{-1}	=	=	=	−0.874
	6061	−0.849	8.172×10^{-6}	2.479×10^{-1}	=	=	=	−0.838
	weld	−1.237	1.490×10^{-6}	4.311×10^{-2}	−1.16	−0.756	1.651×10^{-6}	−0.820
Na_2So_4 0.5 M	5083	−1.229	5.786×10^{-6}	6.541×10^{-2}	−1.084	−0.481	1.345×10^{-5}	−0.796
	6061	−0.849	3.474×10^{-6}	4.856×10^{-2}	−0.75	−0.3		−0.710
	weld	−1.151	6.875×10^{-7}	1.989×10^{-2}	−1.111	−0.523	1.016×10^{-6}	−0.691

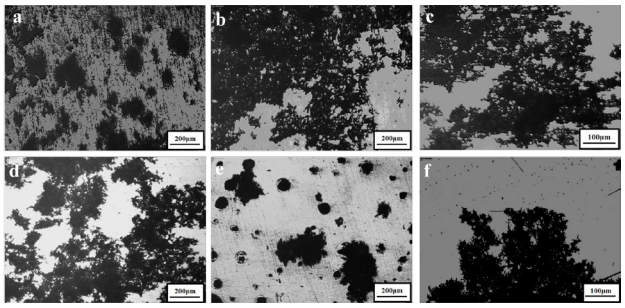

Fig. 4 OM of dissimilar welded joint after corrosion test in NaCl solution (a) welding zone with fine, dispersed inclusions, (b) AA5083-H321 plate, (c) AA6061-T6 stud. OM of dissimilar welded joint after corrosion test in Na_2SO_4 solution (d) welding zone with coarse, interconnected inclusions, (e) AA5083-H321 plate, (f) AA6061-T6 stud.

The polarization curves of the AA5083-H321, AA6061-T6, and dissimilar welded joints in ASTM seawater solution are shown in Fig. 5. The results (Fig. 5 and Table 1) indicate that the corrosion potential of the welded alloy is more than that of the two other alloys (6061 and 5083). Furthermore, the breakdown potential (Eb) values of the passive layers for the three types of alloys (5083, 6061, and welded joints) are approximately convergent (−0.74, −0.74, and −0.8 V, respectively). Additionally, until the potential reaches the pitting potential, the polarization immediate density does not change significantly as a function of the passivation film generated on the samples. The current density begins to rapidly increase at this point, raising the possibility of passivation film breakage or pitting corrosion. Also, the extent of the passive layer for AA6061-T6 is higher than that of the other two studied types of alloys (i.e., 6061 < 5083 < weld). This behavior indicates that the 6061 alloy has a thicker oxide layer than that of the 5083 and weld alloys under these conditions. This is due to the chemical composition of AA6061-T6. It is worth mentioning that, according to our results, the corrosion average of 5083 Al alloy is higher than that of the 6061 and welded alloys.

The polarization curves of the different welded joints, AA5083-H321, and AA6061-T6 in a 3.5 wt.% NaCl solution are displayed in Fig. 6. As can be seen in Table 1, there is a consistent corrosion potential value for both Al alloys (6061 and 5083). The resistance of the material is stable because of the low current density value, and its value is subsequently fixed, meaning that a passive film forms on the alloy surface; however, when the current density is faster this indicates the breakdown of the passive film. The same behavior is shown by AA5083-H321 and AA6061-T6 in this media (i.e., no passive layer appears and the two alloys behave as active metals in this aggressive environment due to the presence of Cl- ions in the solution). The breakdown potential (Eb) of the passive layer is approximately −0.75 V. As a result, this welded alloy has better corrosion resistance than the other two studied alloys under these conditions. This is most probably due to the behavior of the welded region in the surrounding media. Additionally, the corrosion rate of the two Al alloys (6061 and 5083) is higher than that of the welded zone.

Fig. 7 shows the different behaviors of the studied alloys in the Na_2SO_4 solution. For AA5083-H321, there are two passive regions, starting from Epp = −1.084, Eb = −0.48 V and Epp = −0.25, Eb = 0.7 V, respectively. This means that this alloy has the ability to reform the oxide layer on the surface and protect itself against this particular environment.

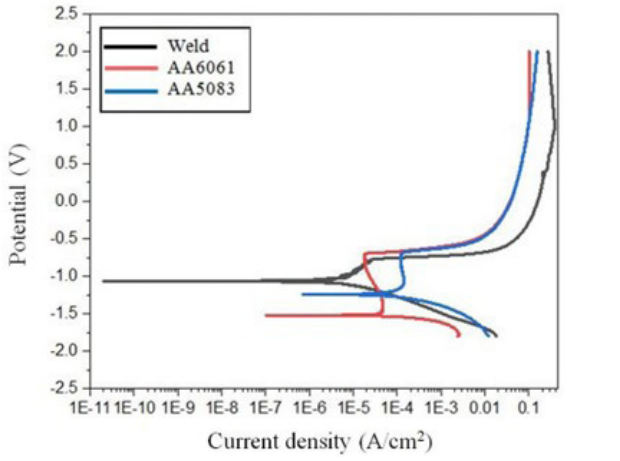

Fig. 5 Polarization curves of (5083, 6061 and weld) Al alloys at static condition in sea water solution

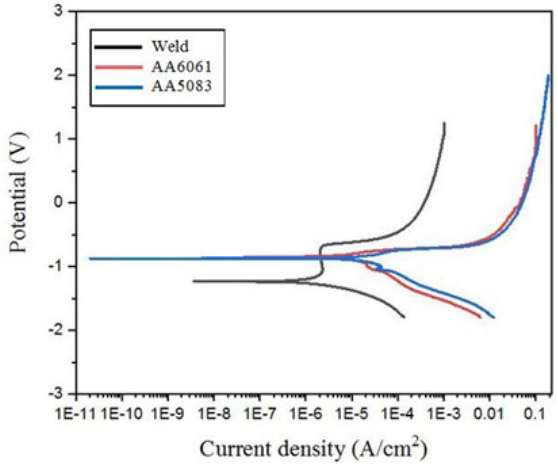

Fig. 6 Polarization curves of (5083, 6061 and weld) Al alloys at static condition in (3.5 NaCl) solution

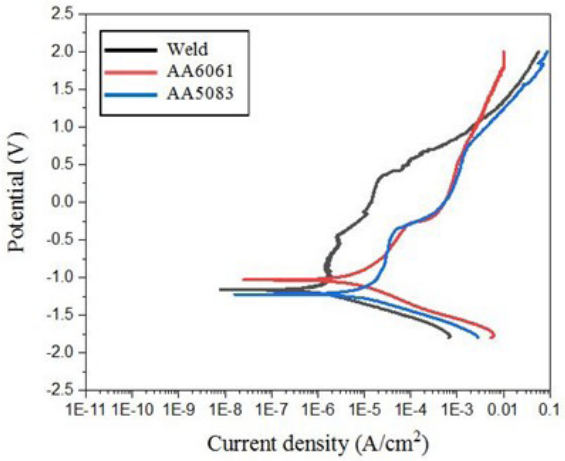

Fig. 7 Polarization curves of (5083, 6061 and weld) Al alloys at static condition in (0.5M Na_2SO_4) solution

For both the 6061 alloy and the welded joint, the passive region started from Epp = −0.75 V, −1.11 V and the breakdown potential was Eb = −0.3 V, 0.375 V. It is noteworthy that the welded alloy has better corrosion resistance, according to the results obtained (lower corrosion rate values), than the other two alloys (5083 and 6061).

The corroded surface was utilized to create an elemental map (Fig. 8), and it was discovered that in addition to O, Na, and Cl, the surface's composition comprised Al, C, Mn, Mg, Fe, and Cr. The ASTM alloy contains the first six elements, and the presence of Cu can be attributed to the use of copper wire in the process of attaching the sample to the corrosion test cell. Finally, the sample was immersed in a salt solution, which resulted in the presence of Na and Cl.

Notably, the presence of oxygen on the map indicates that corrosion has caused metallic oxides to form on the surface. Several metallic oxides can form as a result of the presence of four distinct metals, and the identities of the metallic oxides were ascertained using the Gibbs free energy values. The numbers gathered from traditional thermodynamics indicate that the more stable the oxide, the smaller the value of Gibbs free energy.

Fig. 9 and Table 2 display the findings of the EDX examination of the corroded welding region in ASTM seawater. This table makes it clear that there is a significant concentration of aluminium and oxygen in the corrosion product. The delivery of elements on the corroded surface was ascertained using EDX spectroscopy in order to further validate the elemental mapping results. In accordance

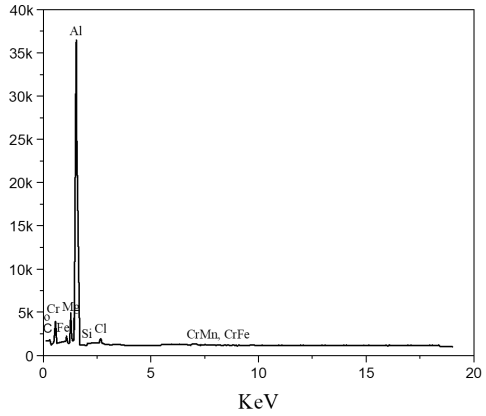

Fig. 9 The EDX spectrum was collected by scanning the corroded surface

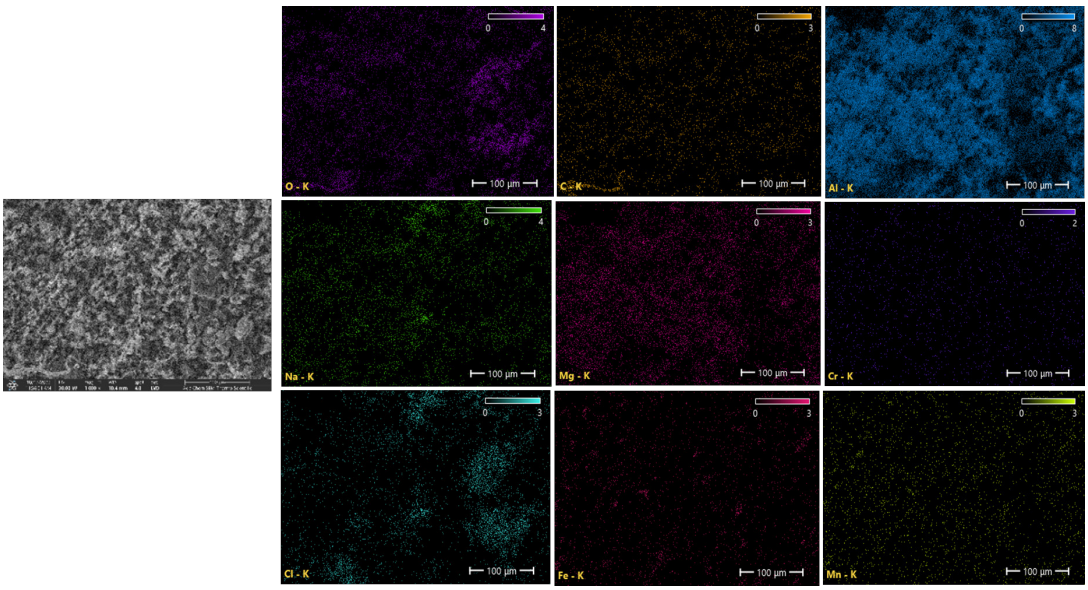

Fig. 8 Elemental mapping of the corroded area confirming the presence of the ASTM seawater elements along with Sodium (Na), Chlorine (Cl), and Oxygen (O) as a result of the corrosion reaction

Table 2 EDX quantification results of dissimilar weldments in ASTM seawater

Element	Atomic %	Atomic % Error	Weight %	Weight % Error
C	23.2	0.4	13.6	0.2
O	29.5	0.4	23.1	0.3
Na	1.8	0.0	2.0	0.1
Mg	2.2	0.0	2.6	0.1
Al	41.1	0.2	54.2	0.2
Si	0.3	0.0	0.4	0.1
Cl	1.2	0.0	2.1	0.0
Cr	0.1	0.0	0.4	0.0
Mn	0.3	0.0	0.8	0.1
Fe	0.3	0.0	0.9	0.1

with the elemental mapping results, Fig. 9 shows that Al, Cr, C, Mn, Mg, Si, Fe, O, and Cl all exhibit strong peaks with high intensity. The identification of iron oxide as the metal oxide that developed on the disc's surface is further supported by the identification of the peak with the highest intensity, which was associated with iron and aluminium. Additionally, the presence of manganese and oxygen on the surface is revealed by another abrupt, powerful peak, which also suggests the development of manganese dioxide on the corroded surface.

The XRD analysis of the dissimilar stud weldments after the corrosion test in ASTM seawater, 3.5% NaCl, and 0.5M Na_2SO_4 are shown in Figs. 10, 11, and 12, respectively. The main phase of the dissimilar weldments in the three different solutions is aluminum hydroxide Al $(OH)_3$. Fig. 1 shows the XRD results in ASTM seawater. In addition to Al $(OH)_3$, there are three phases that exist on the weldment surface: NaCl, Na_2SO_4, and $Al_{19}Fe_4MnSi_2$. The XRD results of the weldment in 3.5% NaCl in Fig. 11 show the formation of NaCl and $Fe_{0.4}Mg_{0.6}O$ phases

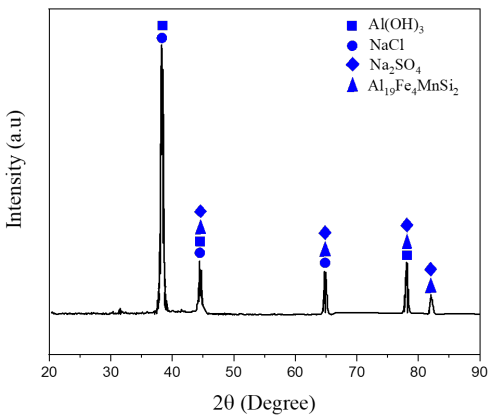

Fig. 10 XRD of AA5083-H321/AA6061-T6-T6 in 0.5M Na_2SO_4 solution

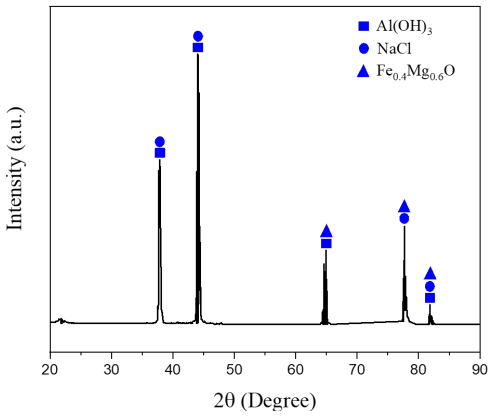

Fig. 11 XRD of AA5083-H321/AA6061-T6-T6 in 3.5% NaCl solution

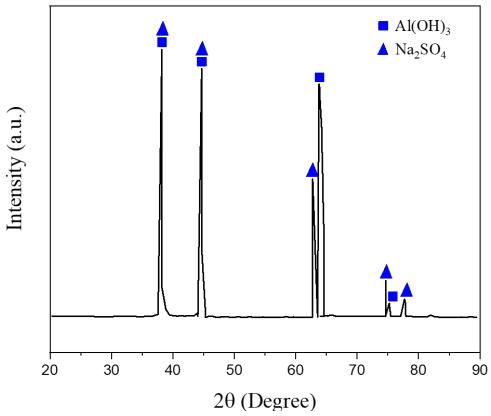

Fig. 12 XRD of AA5083-H321/AA6061-T6-T6 in 0.5M Na_2SO_4 solution

besides the aluminum hydroxide Al $(OH)_3$. The $Fe_{0.4}Mg_{0.6}O$ phase has fewer peaks than that of Al $(OH)_3$ and NaCl. Al $(OH)_3$ and Na_2SO_4 are thus the main phases of the dissimilar weldment surfaces in the Na_2SO_4 solution.

The three-dimensional finite element analysis took the plate geometry into account. In the current investigation, the material's characteristics were assumed to be E = 130 GPa, v = 0.3, and D = 2.6 × 103kg/m^3, where E, v, and D represent density, Poisson's ratio, and Young's modulus, respectively.

The FE standard code in COMSOL was used to model the issue once the base metal (plate) was sent to the probe. The COMSOL code's element type "SIZE", a three-dimensional higher-order eight-node element with two degrees of freedom on each node (translations in the nodal *x*, *y*, and *z* directions), was used to generate the mesh for the plate. The capacity to produce a triangle element and quadratic displacement behaviour are required at the weld tip locations. Singular components were considered at each field of the welding face's tip, modelled using a new mesh, in light of the unique nature of the field of stress in the vicinity of the welding zone. Fig. 13(a) illustrates a characteristic AA5083-H321/AA6061-T6 model of a welded joint.

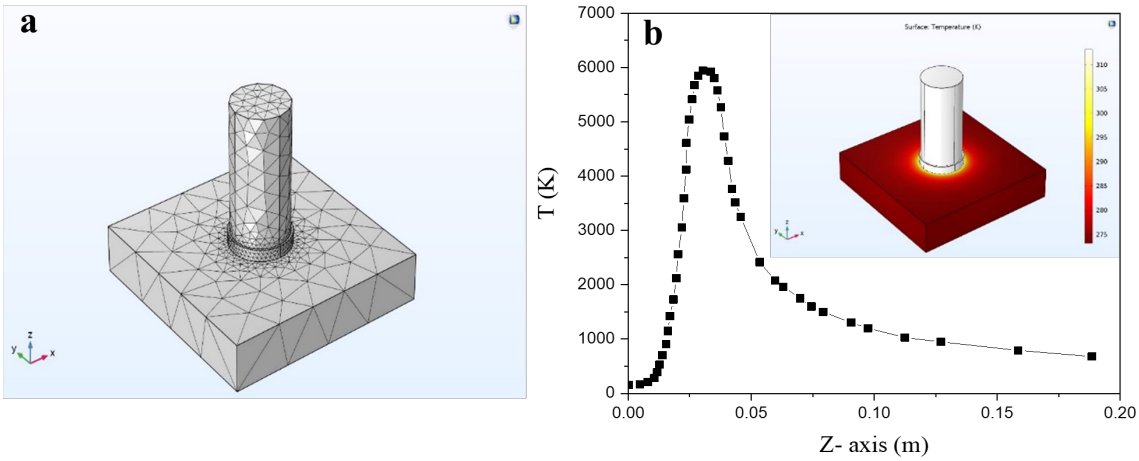

Fig. 13 (a) The symmetry of the FE model of the welding plate, (b) the dimensions of the melted zone compared for constant and temperature-dependent material properties

Fig. 13(b) compares the melted zone dimensions and thermal history along the joint line to emphasize how crucial accurate data are to precisely simulate the length of the melted zone as well as the cooling temperatures. The parametric study of the influence of the welding heat input on the melted zone dimensions was performed, and it was noticed that the melted zone was equal for all surfaces of the base material.

The impact of the disc radii on the local current density for the welding joint surface is shown in Fig. 14. The corrosion dimensional expansion in the AA5083-H321/A6061-T6 electrode may be the cause of the observed rise in local current density with disc radius. However, this effect should be seen from the edges, indicating that the local current density sharply decreases as one gets closer to the disc borders. The results show that edges or defects may be places where corrosion starts. Additionally, it is possible to see the streamlining of the electrolyte current density for the welding joint surface.

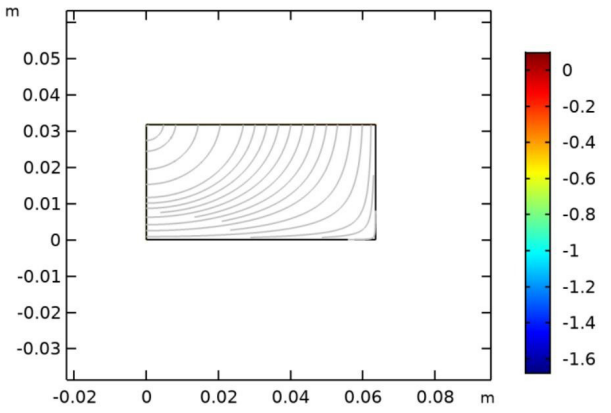

Fig. 14 Local current density vs. disc radii for 3.5%NaCl electrolyte

4 Conclusion

Stud-welded joints of AA5083-H321/AA6061-T6 passivate spontaneously in Na_2SO_4, 3.5% NaCl and ASTM seawater. The corrosion resistance of the dissimilar weldment in Na_2SO_4 solution increased, but it decreased by 3.5% NaCl and was even worse in ASTM seawater. It was noted that the corrosion rate was faster when the material was immersed in ASTM seawater, as noted by the SEM and OM investigations. The corrosion immediate density generally increased, showing a linear relationship with the change in solution. Passive film thickness and pit size were immerged-dependent. The shape of the polarization curve was different from one material to another, and depended upon the type of solution. The results demonstrated that testing DASW joints in a Na_2SO_4 solution yielded a high corrosion resistance and rate, with the resulting pits characterized as thin, sparse, and hemisphere-like. In contrast, lower corrosion resistance and more pronounced pits were observed when the experiments were conducted in 3.5% NaCl and ASTM seawater. Regarding the impact of solution type on the corrosion behaviour of stud-welded AA5083-H321/AA6061-T6 joints, the numerical simulation results using COMSOL software closely match the experimental data.

References

[1] Fallah, V., Langelier, B., Ofori-Opoku, N., Raeisinia, B., Provatas, N., Esmaeili, S. "Cluster evolution mechanisms during aging in Al–Mg–Si alloys", Acta Materialia, 103, pp. 290–300, 2016. https://doi.org/10.1016/j.actamat.2015.09.027

[2] Davis, J. R. "Physical Metallurgy of Aluminum Alloys", In: Davis, J. R. (ed.) Metals Handbook Desk Edition, ASM International, 1998, pp. 437–442. ISBN: 978-1-62708-199-3 https://doi.org/10.31399/asm.hb.mhde2.a0003124

[3] Kuchariková, L., Liptáková, T., Tillová, E., Kajánek, D., Schmidová, E. "Role of Chemical Composition in Corrosion of Aluminum Alloys", Metals, 8(8), 581, 2018. https://doi.org/10.3390/met8080581

[4] Qbau, N., Nam, N., Hien, N., Ca, N. "Development of light weight high strength aluminum alloy for selective laser melting", Journal of Materials Research and Technology, 9, pp. 14075–14081, 2020. https://doi.org/10.1016/j.jmrt.2020.09.088

[5] Cui, L., Guo, M., Peng, X., Zhang, Y., Zhang, J., Zhuang, L. "Influence of Pre-deformation on the Precipitation Behaviors of Al-Mg-Si-Cu Alloy for Automotive Application", Acta Metallurgica Sinica, 51(3), pp. 289–297, 2015. https://doi.org/10.11900/0412.1961.2014.00348

[6] Benkherbache, H., Amroune, S., Zaoui, M., Mohamad, B., Silema, M., Saidani, H. "Characterization and mechanical behaviour of similar and dissimilar parts joined by rotary friction welding", Engineering Solid Mechanics, 9(1), pp. 23–30, 2021. https://doi.org/10.5267/j.esm.2020.6.002

[7] Jebaraj, A. V., Aditya, K. V. V., Kumar, T. S., Ajaykumar, L., Deepak, C. R. "Mechanical and corrosion behaviour of aluminum alloy 5083 and its weldment for marine applications", Materials Today: Proceedings, 22, pp. 1470–1478, 2020. https://doi.org/10.1016/j.matpr.2020.01.505

[8] Rondinella, A., Andreatta, F., Dorbolò, L., Offoiach, R., Capurso, G., Buffa, G., Campanella, D., Fedrizzi, L. "Study of the Corrosion Behaviour of Welded Systems for Marine Industry Applications", In: Technology and Science for the Ships of the Future, IOS Press, 2022, pp. 78–85. ISBN: 978-1-64368-296-9 https://doi.org/10.3233/PMST220011

[9] Singh, R., Venkatesh, V., Kumar, V. "Corrosion: Critical Challenge in Wider Use of Magnesium Alloys", Metals, 8(2), 127, 2018. https://doi.org/10.3390/met8020127

[10] Al-Abboodi, H., Fan, H., Mahmood, I. A., Al-Bahrani, M. "Experimental Investigation and Numerical Simulation for Corrosion Rate of Amorphous/Nano-Crystalline Coating Influenced by Temperatures", Nanomaterials, 11(12), 3298, 2021. https://doi.org/10.3390/nano11123298

[11] Ashok, J., Gupta, A. K. S. "Parametric effect on mechanical, microstructural and corrosion behaviour of friction stir welded AA5083-AA7075 alloys", International Journal on Interactive Design and Manufacturing (IJIDeM), 18(6), pp. 3849–3860, 2024. https://doi.org/10.1007/s12008-024-01850-x

[12] Chen, Z., Li, S., Hihara, L. H. "Electrochemical and mechanical behaviors of dissimilar friction stir welding between 5086 and 6061 aluminum alloy", [preprint] arXiv, 13 January 2018. https://doi.org/10.48550/arXiv.1802.03460

[13] Won, S., Seo, B., Park, J. M., Kim, H. K., Song, K. H., Min, S. H., Ha, T. K., Park, K. "Corrosion behaviors of friction welded dissimilar aluminum alloys", Materials Characterization, 144, pp. 652–660, 2018. https://doi.org/10.1016/j.matchar.2018.08.014

[14] Öteyaka, M. Ö., Ayrtüre, H. "A study on the corrosion behavior in sea water of welds aluminum alloy by shielded metal arc welding, friction stir welding and gas tungsten arc welding", International Journal of Electrochemical Science, 10(10), pp. 8549–8557, 2015. https://doi.org/10.1016/S1452-3981(23)11118-7

[15] Sinhmar, S., Dwivedi, D. K. "A study on corrosion behavior of friction stir welded and tungsten inert gas welded AA2014 aluminium alloy", Corrosion Science, 133, pp. 25–35, 2018. https://doi.org/10.1016/j.corsci.2018.01.012

[16] Bocchi, S., Cabrini, M., D'Urso, G., Giardini, C., Lorenzi, S., Pastore, T. "The influence of process parameters on mechanical properties and corrosion behavior of friction stir welded aluminum joints", Journal of Manufacturing Processes, 35, pp. 1–15, 2018. https://doi.org/10.1016/j.jmapro.2018.07.012

[17] Shamsudeen, S., Dhas John, E. R. "Effect of welding on pitting and intergranular corrosion behavior of marine grade aluminum alloy", Materials Performance and Characterization, 8(4), pp. 555–570, 2019. https://doi.org/10.1520/MPC20180118

[18] Ujjwal, K., Al-Saadi, S., Das, A. K., Raman, R. S. "Corrosion and stress corrosion cracking characteristics of 4043 aluminium alloy fabricated through directed energy deposition process", Journal of Alloys and Compounds, 976, 173154, 2024. https://doi.org/10.1016/j.jallcom.2023.173154

[19] Maqbool, A., Zaman Khan, N. "Microstructure and corrosion behavior of thermo-mechanically processed rare earth Mg alloy: Effect of friction stir processing", Materials Letters, 359, 135934, 2024. https://doi.org/10.1016/j.matlet.2024.135934

[20] Deepa, P., Padmalatha, R. "Corrosion behaviour of 6063 aluminium alloy in acidic and in alkaline media", Arabian Journal of Chemistry, 10, pp. S2234–S2244, 2017. https://doi.org/10.1016/j.arabjc.2013.07.059

[21] Yong, P., Changbin, S., Yadong, Z., Ying, C. "Comparison of electrochemical behaviors between FSW and MIG joints for 6082 aluminum alloy", Rare Metal Materials and Engineering, 46(2), pp. 344–348, 2017. https://doi.org/10.1016/S1875-5372(17)30092-9

[22] Wahid, M. A., Siddiquee, A. N., Khan, Z. A. "Aluminum alloys in marine construction: characteristics, application, and problems from a fabrication viewpoint", Marine Systems & Ocean Technology, 15(1), pp. 70–80, 2020. https://doi.org/10.1007/s40868-019-00069-w

[23] Gadallah, E. A., El Aal, M. I. A., Mohamed, A. Y., El-Fahhar, H. H. "Effects of filler on the microstructure and corrosion of similar and dissimilar gas inert tungsten arc welding aluminum alloys joints", Scientific Reports, 13(1), 19011, 2023. https://doi.org/10.1038/s41598-023-44421-y

[24] Nishikawa, W. "The principle and application field of stud welding", Welding International, 17(9), pp. 699–705, 2003. https://doi.org/10.1533/wint.2003.3170

[25] Soltanzadeh, H., Hildebrand, J., Kraus, M., Asadi, M. "Modelling of a Stud Arc Welding Joint for Temperature Field, Microstructure Evolution and Residual Stress", In: Proceedings of the ASME 2016 Pressure Vessels and Piping Conference, Vancouver, British Columbia, Canada, 2016, V06BT06A002. ISBN: 978-0-7918-5043-5 https://doi.org/10.1115/PVP2016-63285

[26] Abass, M. H., Alali, M. S., Abbas, W. S., Shehab, A. A. "Study of solidification behaviour and mechanical properties of arc stud welded AISI 316L stainless steel", Journal of Achievements in Materials and Manufacturing Engineering, 97(1), pp. 5–14, 2019. https://doi.org/10.5604/01.3001.0013.7944

[27] Razzaq, M. K. A., Abood, A. N. "Effect of arc stud welding parameters on the microstructure and mechanical properties of AA6061-T6 and AA5083-H321 aluminium alloys", Journal of Achievements in Materials and Manufacturing Engineering, 108(1), pp. 24–34, 2021.
https://doi.org/10.5604/01.3001.0015.4796

[28] Nikseresht, Z., Karimzadeh, F., Golozar, M. A., Heidarbeigy, M. "Effect of heat treatment on microstructure and corrosion behavior of Al6061 alloy weldment", Materials & Design (1980-2015), 31(5), pp. 2643–2648, 2010.
https://doi.org/10.1016/j.matdes.2009.12.001

[29] Liu, Z., Han, P., Wang, W., Guan, X., Wang, Z., Fang, Y., Qiao, K., Ye, D., Cai, J., Xie, Y., Wang, K. "Microstructure, mechanical properties, and corrosion behavior of 6061Al alloy prepared by cold spray-friction stir processing composite additive manufacturing", Transactions of Nonferrous Metals Society of China, 33(11), pp. 3250–3265, 2023.
https://doi.org/10.1016/S1003-6326(23)66331-9

[30] Gnedenkov, A. S., Sinebryukhov, S. L., Mashtalyar, D. V., Imshinetskiy, I. M., Vyaliy, I. E., Gnedenkov, S. V. "Effect of microstructure on the corrosion resistance of TIG welded 1579 alloy", Materials, 12(16), 2615, 2019.
https://doi.org/10.3390/ma12162615

[31] Liu, S., Yi, T., Fang, C., Jiang, G., Dai, X. "Enhancing corrosion resistance of the nugget in a 2519-T87 aluminum alloy friction stir welded joint via tungsten inert gas arc", Science and Technology of Welding and Joining, 29(1), pp. 52–60, 2024.
https://doi.org/10.1177/13621718231220878

[32] Abdelmalek, E., Amroune, S., Zaoui, M., Mohamad, B., Bouchoucha, A. "Experimental investigations of surface wear by dry sliding and induced damage of medium carbon steel", Diagnostyka, 22(2), pp. 3–10, 2021.
https://doi.org/10.29354/diag/134116

[33] Siguerdjidjene, H., Houari, A., Madani, K., Amroune, S., Mokhtari, M., Mohamad, B., Chellil, A., Merah, A., Campilho, R. "Predicting damage in notched functionally graded materials plates through extended finite element method based on computational simulations", Frattura ed Integrità Strutturale, 18(70), pp. 1–23, 2024.
https://doi.org/10.3221/IGF-ESIS.70.01